Journal of Anatomy / Early View

Original Paper

Morphological correspondence between brain and endocranial surfaces in mice exposed to undernutrition during development

Noelia Bonfili, Jimena Barbeito-Andrés, Valeria Bernal, Benedikt Hallgrímsson, Paula N. Gonzalez

First published: 07 February 2022
https://doi.org/10.1111/joa.13639

Abstract

The morphological changes of the brain and the skull are highly integrated as a result of shared developmental pathways and different types of interactions between them. Shared developmental trajectories between these two structures might be influenced by genetic and environmental factors. Although the effect of environmental factors on neural and craniofacial traits has been extensively studied, less is known about the specific impact of stressful conditions on the coordinated variation between these structures. Here, we test the effect of early nutrient restriction on morphological correspondence between the brain and the endocast. For this purpose, mice exposed to protein or calorie-protein restriction during gestation and lactation were compared with a control group in which dams were fed standard food ad libitum. High-resolution images were obtained after weaning to describe brain and endocranial morphology. By magnetic resonance imaging (MRI), brain volumes were obtained and endocasts were segmented from skull reconstructions derived from micro-computed tomography (microCT). Brain and endocranial volumes were compared to assess the correspondence in size. Shape changes were analyzed using a set of landmarks and semilandmarks on 3D surfaces. Results indicated that brain volume is relatively less affected by undernutrition during development than endocast volume. Shape covariation between the brain and the endocast was found to be quite singular for protein-restricted animals. Procrustes distances were larger between the brain and the endocast of the same specimens than between brains or endocasts of different animals, which means that the greatest similarity is by type of structure and suggests that the use of the endocast as a

direct proxy of the brain at this intraspecific scale could have some limitations. In the same line, patterns of brain shape asymmetry were not directly estimated from endocranial surfaces. In sum, our findings indicate that morphological variation and association between the brain and the endocast is modulated by environmental factors and support the idea that head morphogenesis results from complex processes that are sensitive to the pervasive influence of nutrient intake.

Open Research

DATA AVAILABILITY STATEMENT

Data is available as Supporting Information as well as a brief description of the scripts that were applied.

Supporting Information

Filename	Description
joa13639-sup-0001-Supinfo1.docx Word 2007 document , 231.9 KB	**Data S1**

Please note: The publisher is not responsible for the content or functionality of any supporting information supplied by the authors. Any queries (other than missing content) should be directed to the corresponding author for the article.

TITLE

Morphological correspondence between brain and endocranial surfaces in mice exposed to undernutrition during development

Bonfili N[1], Barbeito-Andrés J[1*], Bernal V[2], Hallgrímsson B[3], Gonzalez PN[1]

1. Estudios en Neurociencias y Sistemas Complejos (CONICET - Hospital El Cruce - Universidad Nacional Arturo Jauretche). Buenos Aires, Argentina.
2. CONICET. División Antropología, Facultad de Ciencias Naturales y Museo, Universidad Nacional de La Plata. Buenos Aires, Argentina.
3. Department of Cell Biology & Anatomy, University of Calgary. Calgary, Canada.

CORRESPONDENCE TO: *Barbeito-Andrés J. barbeito@fcnym.unlp.edu.ar

SHORT RUNNING PAGE HEADING: Brain and endocast morphology after undernutrition

ABSTRACT

The morphological changes of the brain and the skull are highly integrated as a result of shared developmental pathways and different types of interactions between them. Shared developmental trajectories between these two structures might be influenced by genetic and environmental factors. Although the effect of environmental factors on neural and craniofacial traits has been extensively studied, less is known about the specific impact of stressful conditions on the coordinated variation between these structures. Here, we test the effect of early nutrient restriction on morphological correspondence between the brain and the endocast. For this purpose, mice exposed to protein or calorie-protein restriction during gestation and lactation were compared with a control group in which dams were fed standard food *ad libitum*. High resolution images were obtained after weaning to describe brain and endocranial morphology. By magnetic resonance imaging (MRI), brain volumes were obtained and endocasts were segmented from skull reconstructions derived from micro computed tomography (microCT). Brain and endocranial volumes were compared to assess the correspondence in size. Shape changes were analyzed using a set of coordinate landmarks and semilandmarks on 3D surfaces. Results indicated that brain volume is relatively less affected by undernutrition during development than endocast volume. Shape covariation between the brain and the endocast was found to be quite singular for protein restricted animals. Procrustes distances were larger between the brain and the endocast of the same specimens than between brains or endocasts of different animals, which means that the greatest similarity is by type of structure and suggests that the use of the endocast as a direct proxy of the brain at this intraspecific scale could have some limitations. In the same line, patterns of brain shape asymmetry were not directly estimated from endocranial surfaces. In sum, our findings indicate that morphological variation and association between the brain and the endocast is modulated by environmental factors and support the idea that head morphogenesis results from complex processes that are sensitive to the pervasive influence of nutrient intake.

KEYWORDS: Magnetic Resonance Imaging, Computed Tomography, Geometric Morphometrics, Brain plasticity, Morphological integration, Paleoneurology

INTRODUCTION

The brain and the skull are highly integrated over development and evolution (Hanken and Thorogood, 1993; Richtsmeier et al., 2006; Nieman et al., 2012; Richtsmeier and Flaherty, 2013). However, shared developmental trajectories between both structures might be influenced by different factors that unfold over ontogeny. Differences in patterns of morphological coordinated variation between the brain and the neurocranium among mouse strains from diverse backgrounds (Hill et al., 2013; Motch Perrine et al., 2017) suggest that genetic factors can modulate the relationship between brain and skull. A question that remains to be studied is to what extent environmental factors in general and nutrient restriction in particular influence the morphological correspondence between these structures.

Nutrition plays a key role in development. Several growth and maturation processes depend on the direct or indirect influence of macro and micronutrients that are available during early ontogeny (Nijhout, 2003; Prado and Dewey, 2014). Energy and protein restriction were found to have systemic effects, affecting a large variety of tissues, organs and systems (Ulijaszek, 1996; Brameld, 2004; Alamy and Bengelloun, 2012; Gonzalez et al., 2016; Bourke et al., 2019). The impact of nutritional deficiency is a matter of interest not only because of its consequences but also due to the fact it is a common factor in human populations (Black et al., 2008) as well as in many ecosystems for wild animals (Barboza et al., 2009).

Different experimental designs have shown that the growth of skull bones is sensitive to undernutrition in early stages of development (Pucciarelli and Oyhenart, 1987; Dressino and Pucciarelli, 1997; Gonzalez et al., 2016), being the magnitude of the effect dependent on the timing and duration of the environmental perturbation (Gonzalez et al., 2011). Particularly, maternal protein restriction during gestation not only leads to size reduction of the skull in the offspring, after accounting for body size and maternal effect, but also to differences in the shape of craniofacial structures (Gonzalez et al., 2016). Regarding brain development, there is a large corpus of evidence suggesting that nutrient restriction affects crucial processes such as neurogenesis and leads to developmental impairment (Georgieff, 2007; Prado and Dewey, 2014; Hunter et al., 2016), although brain growth was found to be relatively buffered by a preferential allocation of resources (nutrient and oxygen) to this organ in restrictive contexts (Reichling and German, 2000; Gonzalez et al., 2016).

In this study, we analyze the brains and endocasts of young adult mice experimentally exposed to nutrient restriction during gestation and lactation to assess how changes in brain size and shape induced by this environmental factor are related to variation in the endocast. Although the brain and the skull are integrated, it is expected to find differential responses to nutritional restriction due to

specific developmental pathways and processes that affect each structure. If there is a differential response to nutritional restriction of the cranium and the brain, then their coordinated growth and development could be altered. Our earlier finding that maternal protein restriction is associated with reduced covariation between skull and brain morphology in mice is in line with these expectations (Barbeito-Andrés et al., 2016). However, most studies using experimental designs to model nutrient deficits have focused on ectocranial traits, while the endocranial morphology has not been systematically addressed. By analyzing changes in brain and endocranial morphology in controlled conditions, we aim to contribute to understanding the developmental dynamics of both structures under the influence of a disrupting environmental factor. As a correlate, our study will contribute to the discussion about the accuracy of using endocasts to assess brain variation in size, shape and surface structural features when soft tissues are not available at an intraspecific scale.

MATERIAL AND METHODS

Sample and image acquisition

The sample was composed of C57BL/6J mice divided into three different experimental groups according to the diet consumed by their mothers during prenatal and early postnatal life: control (Co), moderate low calorie-protein (LCP) and severe low-protein (LP). For Co animals, dams had *ad libitum* access to a standard 20% protein diet with a caloric proportion of 3.8 Kcal/g. The LP group was fed with a protein-restricted diet (6%) in the form of casein and DL-Methionine with the same amount of calories as the control diet from the day of pregnancy confirmation (E0) (Harlan Teklad, Madison). Co and LP groups received the corresponding diets until the weaning of the pups in the day 20 of postnatal life (P20). In the case of LCP diet, dams started receiving 80% of the control diet since the tenth day of the pregnancy (E10). After weaning and until euthanasia, all experimental groups were fed the same standard diet. At day 34 of postnatal life (P34) the offspring was deeply anesthetized and specimens were perfused with 4% paraformaldehyde (PFA) to fix tissues. Contrast agents were not used to avoid this source of shrinkage of the soft tissues. All procedures were executed following the guidelines of the Canada Council on Animal Care (UCalgary) and with the approval of the Committee for the Care and Use of Experimental Animals (CICUAL) of the Faculty of Veterinary of the National University of La Plata (Protocol number 42-2-14P). More details on the experimental design and procedures are available at Barbeito-Andrés et al. (2018).

We analyzed 21 specimens of both sexes from at least 3 different dams by experimental group (Co= 5 males and 3 females, LCP= 3 males and 3 females, and LP= 3 males and 4 females). Males and females were pooled given that we previously reported no significant differences between sexes on body and gross brain size (Barbeito-Andrés et al., 2018). It is worth noting that Co group had a significant larger body weight compared to the other groups (Barbeito-Andrés et al., 2018).

For each specimen, we obtained micro-computed tomography (microCT) images of the skull and magnetic resonance images (MRI) of the brain. Parameters for microCT are isotropic voxel size of 0.035 mm, 55 kVp, 145 µA and 500 projections per 180 degrees, while the parameters used for MRI were T2-weighted echo-gradient sequence, with TE 10 ms and field-of-view 15×15 mm and matrix size of 128×128×30. These acquisition settings resulted in a relatively lower resolution in MRI than microCT scans. In addition, since matrix size is not constant in the three directions, MRIs are not isotropic. In comparison, the voxel size for microCT is 0.035 mm, while the maximal resolution for the MRI voxels is around 0.11 mm. MicroCT images were obtained in a Scanco uCT 35 from the Micro CT Laboratory (University of Calgary, Canada) and MRI was performed with a Bruker 9.4T BioSpec from the Experimental Imaging Centre (University of Calgary, Canada).

Endocast and brain reconstructions

First, skull bones were labelled on microCT images using a thresholding strategy and three-dimensional reconstructions of the skull were obtained as meshes in ply format with Amira software. The endocranial volumes were then segmented using the semi-automatic procedure introduced by Profico et al. (2018). For this purpose, a set of 23 landmarks was digitized on the endocranial surface of cranial bones, as shown in Fig. 1A. These landmarks were used at this processing stage to allow semi-automatic extraction of the endocast but they were not included in the morphometric analyses. The mesh file of the skull together with the coordinates of landmarks were processed with the Automatic Segmentation Tool (AST-3D) method as implemented in R's Arothon and Morpho packages (Schlager, 2017; Profico et al., 2018). The endocast model generated by AST-3D was then post-processed manually in 3D Slicer (Fedorov et al., 2012) to complete missing polygons and remove artifact polygons from the surface (Fig. 1A).

Second, an automatic skull stripping procedure was performed on MRI using the BrainSuite software (Shattuck and Leahy, 2002) in order to define the brain tissue for each specimen and obtain three-dimensional models of the brain (Fig. 1B). After each automatic segmentation, a visual inspection was performed to corroborate accuracy of brain tissue segmentation and, in those cases with minor artifacts, a manual correction was carried out.

Morphometric analyses

To examine the variation in size, we estimated the volume of brains and endocasts expressed in mm^3. Differences in volume among groups were assessed using ANOVA and post-hoc Tukey tests. The coordinated variation of brain and endocast volumes was evaluated by a linear regression. Additionally, the parameters of the linear regression between endocast and brain volume of Co animals were used to estimate the brain volumes for LCP and LP groups from the volume of the endocasts. Differences between observed and estimated values of brain volume were analyzed with the non-parametric Wilcoxon test.

In addition, geometric morphometric techniques were used to study shape variation of the external surfaces of brains and endocasts. For this purpose, a set of 12 curves including 205 landmarks and semilandmarks were digitized in geometrically homologous positions of the brain and the endocast using Landmark Editor (Wiley et al., 2005) (Fig. 1C, Table 1). In order to assess the digitization error, a test for repeatability was performed by the author that digitized the landmarks in the study (NB) and the results are available as Supporting Information (Fig. S1, S2, Table S1). Semilandmarks of

each structure were slid using a bending energy criterion (Gunz et al., 2005) and a generalized Procrustes analysis was performed.

The magnitude of shape differences between the brain and endocast of each specimen was compared to the shape differences among specimens for each structure. This comparison is informative on the reliability of endocasts as proxies of brain shape variation in an intraspecific context. With this aim, we obtained the Procrustes distance between the brain of each specimen and its corresponding endocast and the pairwise Procrustes distances between configurations of each structure (brain and endocast) within each experimental group. These measures of distance allow the comparison of the magnitude of intra-group shape similarity/dissimilarity in the brain and the endocast with the intra-specimen similarity between structures. ANOVA and Tukey post-hoc tests were then performed to compare Procrustes distances between brains and endocasts, and between experimental groups. Based on the brain-endocast distances, the specimen that was the closest to the mean Procrustes distance in each group was chosen to illustrate its shape using morphings.

In order to further explore the shape variation of brains and endocasts, a Principal Component Analysis (PCA) was performed on brain shape coordinates, and a separate PCA was carried out on the endocast shape coordinates. PCA is commonly used in geometric morphometrics to find a reduced number of dimensions that represent most of the variation in a dataset, which is particularly useful for the analysis of large sets of variables with few specimens, as is usually the case when 3D semilandmarks are used (Gunz and Mitteroecker, 2013). The ordinations of specimens along the first two principal components obtained for each structure were compared using a PROTEST analysis (Peres-Neto and Jackson, 2001). The sum of the squared residuals between ordinations after superimposition was estimated as a measure of association as implemented in vegan package for R (Oksanen et al., 2015).

Patterns of shape covariation between the brain and the endocast were explored using a Two Block Partial Least Squares (PLS) analysis, which is a singular value decomposition of the covariance matrix (Rohlf and Corti, 2000). We focused on the first PLS axis since it accounts for the largest amount of inter-block covariation. As well, shape variation along PLS1 was illustrated using the same procedure than for PCA. PLS1 extreme configurations (negative and positive) for brain and endocast blocks were morphed using a mean endocast surface as a baseline.

In addition, overall shape asymmetry was estimated for each specimen as the square root of the overall sum of the squared differences between the symmetric component and the coordinates of landmarks and semilandmarks after Procrustes superimposition. Finally, PCA on the asymmetric component was performed to visualize the localization of asymmetric shape variation in both the

endocast and the brain. Statistical and morphometric analyses were performed in R version 4.0.2 (R Core Team, 2020) using Geomorph (Adams et al., 2020) and Morpho packages (Schlager, 2017).

Data is available as Supporting Information as well as a brief description of the scripts that were applied.

RESULTS

Nutritional stress has a greater effect on endocast volume than on brain size

ANOVA test showed that brain growth was impaired under nutritional restriction ($F = 19.282$, $p < 0.001$) and pairwise comparisons resulted in significant differences between Co and the two groups of undernourished specimens (Fig. 2A). Similar results were found for the endocasts as the groups also differed in volume ($F = 30.582$, $p < 0.001$), with the endocasts of Co group significantly larger than those of LCP and LP (Fig. 2A). When controlling for litter size, these patterns of differentiation were similar (Table. S2). The brain volume represented 87.428% (±1.908) of the endocranial volume in Co, while this value was larger in LCP (88.077% ±1.456) and LP (88.815% ±1.311).

Changes in endocranial volume were significantly associated with brain size (Pearson correlation coefficient = 0.968, $p < 0.001$), although as expected, endocasts were larger than brains in average (Fig. 2A). The linear regressions between endocast and brain volumes for each experimental group showed large r^2 values for Co and LP groups, whereas the linear function for LCP had a very low fit (Fig. 2B). Based on these results, a linear model was fitted to Co and LP specimens using the endocast volume as the response variable, and brain volume and group as predictors, including the interaction between them. Results indicated that regressions for Co and LP did not differ in slope ($F = 0.131$, $p = 0.724$), although there were differences in their intercepts ($F = 8.431$, $p = 0.014$).

Finally, the brain volume of LCP and LP specimens was larger than the volume estimated from the linear model of endocast and brain volumes for Co, suggesting that nutrient restricted animals have larger brains than the estimated for a given endocast volume (Fig. 2C).

Shape correspondence between the brain and the endocast

The pairwise Procrustes distances between the brain and endocast of each specimen indicate that shape differences between both structures were significantly larger in Co specimens than in LCP, while brain-endocast distances did not differ significantly between Co and LP, or between LCP and LP (Fig. 3A, Table 2). With the purpose of illustrating individual differences between the brain and the endocast, we chose those specimens closer to the average in brain-endocast distance for each group.

In Fig. 3B-D, morphings for Co, LCP and LP derived from these selected specimens are presented. The shape differences between both structures were similar among groups, with endocasts being relatively taller and convexed in the dorsal surface, while brains were dorsally flatter. As well, the limit between the surface corresponding to the cortex and the cerebellum was more rostrally placed in the endocasts (Fig. 3B-D).

In addition, we analyzed whether the magnitude of brain-endocast distances within specimens was similar to the distances among specimens estimated for the brain and the endocast separately. Brain-endocast distances in Co group were larger than distances between specimens in the three experimental groups both for the brain and the endocast (Fig. 3A, Table 2). In other words, there was a closer correspondence in the shape of the same structure (brain or endocast) when different specimens were compared than between the brain and endocast of the same specimen. This scenario was also confirmed for brain-endocast distances in LP, which were larger than brain shape variation within LCP and LP, and than endocast variation within Co and LCP (Fig. 3A, Table 2). In general, the experimental groups presented similar magnitudes of Procrustes distance between specimens both for the brain and the endocast, although brain distances were significantly different between Co and LCP, and endocast distances were significantly larger for LP than for LCP (Fig. 3A, Table 2). This last result suggests that nutrient restriction could promote different patterns of shape variation in the endocast and the brain.

To further analyze shape variation in the brain and the endocast and to detect shared and divergent patterns, PCA on shape coordinates was performed for both structures. The first axis of the PCA on brain shape coordinates accounted for 32.05% of total variation while the PC2 accounted for 13.74%. The three groups overlapped along these two first axes, with a subtle tendency of LP to have more positive values in the PC1 (Fig. 4A). Similarly, the groups overlapped along the PC1 and PC2 of the endocast shape variables, which are associated with the 24.22% and 15.21% of variation, respectively (Fig. 4B). However, the distribution of specimens along the first two PCs of the brain and endocast differ, resulting in a very low correlation (r=0.120, p=0.921, perm=999). Main shape variation for the brain was localized in the lateral curves of the cerebrum that was more expanded and rounded in the frontal section towards the positive PC1 extreme, in the olfactory bulbs that had a more squared shape in positive scores along PC1, and in the region of the cerebellum, which was antero-posteriorly shorter in specimens with negative values for PC1 (Fig. 4A). Most noticeable shape changes described by the PC1 for the endocast were in the lateral curves of the cortex surface, which did not resemble the shape change in the brain, with specimens in the PC1 positive extreme showing lateral expansion but in the middle and caudal parts of the endocast (Fig. 4B).

In order to examine shape covariation between the brain and endocast, a PLS analysis was performed. We found that PLS1 accounted for 47.42% of total covariation and the correlation coefficient obtained for the scores corresponding to the brain and the endocast is large (r = 0.79), although, probably due to the sample size, it is not significant (p = 0.125). Along PLS1, LP specimens tended to occupy the positive values, separated from LCP, which mostly had negative values (Fig. 5A). Although Co overlapped with undernourished groups, it is worth noting that most specimens are placed in negative positions both for the endocast and the brain block (Fig. 5A). For those specimens around negative PLS1 values, brain and endocranial shape presented similarity in the direction and magnitude of associated shape changes. In contrast, towards positive PLS1 values, subtle endocranial variation, especially located in the rostral curves of the part that correspond to the mold of cerebellum was linked to marked shape changes in the brain that included relatively rectangular olfactory bulbs, more rounded rostro lateral cortical surfaces and a more extended surface for the cerebellum (Fig. 5B).

Shape asymmetry in the brain and the endocast

Shape asymmetry of brains and endocasts of each specimen was estimated from their Procrustes coordinates. First, an asymmetry score was obtained as the sum of distances between the symmetric component and the Procrustes shape coordinates. This score, representing the overall shape asymmetry, was similar for the brain and the endocast (t = 1.088, p = 2.002), suggesting a comparable magnitude of global shape asymmetry (Fig. 6A). As is shown in Fig. 6A, groups were largely overlapped and no significant differences were found for inter-group comparisons neither for the brain (F = 0.488, p = 0.622) nor the endocast (F = 0.931, p = 0.412).

To describe the spatial patterns of asymmetric shape variation in both anatomical structures, PCAs on the asymmetric component were performed for the brain and the endocast separately. Shape asymmetric variation did not separate experimental groups, which were largely overlapped along the first two PCs both for the brain and the endocast (Fig. 6B). Asymmetric shape variation summarized by PC1 is presented in Fig. 6B as heatmaps, in which darker colors indicate more asymmetric areas. Both the endocast and the brain presented asymmetric variation in the lateral side of the olfactory bulbs, but main asymmetric patterns differ between both structures. In the endocast, shape asymmetry was localized in the lateral and rostral part of the surface that correspond to the cortex, while in the brain there the asymmetry was more evident in the caudal limit of the cortex and the lateral and middle surface of the cerebrum.

DISCUSSION

The coordinated morphological variation between the brain and the skull has been intensively studied from the seminal experiments that induced alterations in rat brain growth and found that cranial bones changed accordingly in size and shape (Moss and Young, 1960), to recent findings that demonstrate common genetic pathways and molecular mechanisms of mechanotransduction (Yu et al., 2001; Richtsmeier and Flaherty, 2013; Marcucio et al., 2015; Motch Perrine et al., 2017). Altogether, the results of such studies confirm that these tissues develop in a coordinated fashion. The interest on brain and skull interactions along early ontogeny came in part from studies exploring craniofacial dysmorphologies that primarily affect one of these structures and that, as a consequence, impact the other (Richtsmeier and Flaherty, 2013; Motch Perrine et al. 2017). As well, basic developmental biology has tried to understand those mechanisms involved in shared developmental trajectories (Adameyko and Fried, 2016; Marcucio et al., 2011, 2015). Regarding the factors that potentially modulate these mechanisms, antecedents have largely focused on genetic variables (Motch Perrine et al., 2017; Lieberman et al., 2008) or explored ectocranial traits of the skull (Lieberman et al., 2008; Gonzalez et al., 2016; Barbeito-Andrés et al., 2016; Motch Perrine et al., 2017). Here, we approached a relevant environmental factor by studying the morphological correspondence between brain and endocranial traits at an intraspecific scale, which also differs from previous works that established interspecific comparisons (Watanabe et al., 2019).

According to our results, some aspects of morphological correspondence between the brain and the endocast might be influenced by nutrient restriction during prenatal and early postnatal life. Changes in the coordinated patterns of morphological variation could result, at least in part, of a differential response of both structures to the modeled stimulus. First, although there is a global association between endocranial and brain volumes, we found that the brain of undernourished specimens was larger relative to the endocast compared to controls. Even though some influence of the different types of images (microCT and MRI) used to describe each structure and the samples' processing procedures on volume estimation can not be discarded, this effect is expected to be homogenous for all experimental treatments. Moreover, our results are consistent with the hypothesis of brain sparing, which states that under stressful scenarios, nutrients and oxygen are differentially allocated to brain growth (Cohen et al., 2015; Miller et al., 2016). In this line, we previously reported that maternal protein restriction during pregnancy in mice results in fetuses with smaller heads, although larger than expected for their body size (Gonzalez et al., 2016). How these buffering mechanisms affect differentially brain and skull structures were not explored in detail before. In a study that measures postmortem brain size and head circumference in cases of

intrauterine growth restriction, Cooke et al. (1977) also showed that they had larger brains for a given value of head circumference than control infants. Here, we found that even though the size of the endocasts is associated with brain size, there is a relatively differential response from them. It has been proposed that mechanisms responsible for brain sparing are mainly related to circulatory adaptations that derive in a preferred supply of oxygen and nutrients to the brain (Cohen, 2015). Since brain and skull are integrated structures, there is some effect of growth buffering impacting on the skull but, according to our results, the pattern of sparing is not the same for the brain and the endocast, probably due to mechanisms that specifically target brain growth.

Shape coordinated variation was also explored in our study and we found that experimental groups did not differ in their shape, which might be due in part to the sample size. However, the comparison of Procrustes distances for the endocast and brain among groups suggests some differences in the patterns of shape changes in both structures. Covariation between brain and endocranial traits, as shown in the PLS analysis, reflected that some aspects of brain and endocast morphology were decoupled in the low protein treatment group, while the correspondence in the other experimental groups was stronger. Previous studies exploring skull morphology have found that covariation between craniofacial structures could be modulated by genetic factors that affect development (Martinez Abadías et al., 2011), and here we reinforce this idea of plasticity for brain and endocast covariation in a context of nutritional stress. One possible explanation could be related to a subtle decoupling in their developmental schedules and timings. For instance, brain development initiates before cranial bones start their mineralization (Richtsmeier and Flaherty, 2013). Another aspect to consider is the effect of other tissues on the skull and, therefore, on endocast. These stimuli could represent a combination of somatic factors (Gonzalez et al., 2013) and the local effect of the brain, muscles, and other tissues and organs. Accordingly, we found that morphological correspondence between the brain and the endocast was rather limited, with a greater similarity in shape by type of structure (brain or endocast) than between the endocast and the brain of the same specimen.

One of the aspects of shape we particularly analyzed was asymmetry, which was similar in magnitude but not in pattern between the brain and the endocast. It remains to be determined to what extent the divergences we found between the asymmetric patterns of the brain and the endocast are found in other mammalian species and across developmental stages. In humans, comparisons between adult brains and endocranial surfaces revealed that some regions share the asymmetric configuration, while others present significant differences and, at least for these regions, the endocranial surface might not represent brain asymmetry (Fournier et al., 2011).

Our results contribute to discussing the accuracy of endocranial structures as proxies of the brain at different taxonomic levels. Endocasts are widely used to infer brain shape, particularly by applying geometric morphometric tools that allow to explore the shape of smooth external surfaces with very few anatomical landmarks (Neubauer et al., 2010; Aristide et al., 2016; Marugán-Lobón et al., 2016; Scholz et al., 2016; Gómez-Robles et al., 2018; Pereira-Pedro and Bruner, 2018). Using a similar approach to ours, based on comparisons of Procrustes distances, Watanabe et al. (2019) show that brain-endocast difference at the intraspecific level did not significantly differ from variation found among brains or endocasts of the same species. However, the sample composition and design of the referenced study is different from ours since they included specimens of diverse ontogenetic stages.

To conclude, our study shows that the correspondence between the brain and the endocast in some morphological aspects can be modulated by nutritional stress during development, which is a pervasive source of environmental variance (Nijhout, 2003). Previous work on humans suggested that, although the brain and the endocast are tightly integrated, when dissecting some phenotypic features this association is limited and extrapolating changes in one of them based on the other should be more cautious (Alatorre Warren et al., 2019). The results presented here might have implications for natural populations exposed to different environmental perturbations during early ontogeny, which can induce neuroanatomical changes that are not reflected on the endocasts and vice-versa. For instance, brain development was found to be modified in response to perceived predation risk in some fish species, suggesting that plastic changes occur in brain structures under particular environmental conditions (Gonda et al., 2012; Kotrschal et al., 2017). Therefore, the results presented here open a venue for future studies exploring the influence of other sources of environmental perturbations on brain and endocranial morphological correspondence.

ACKNOWLEDGMENTS

This work is partially funded by ANPCyT PICT 2017-2497 and PICT 2018-4113. We thank Antonio Profico for helping in the implementation of automatic endocast extraction.

AUTHORS CONTRIBUTIONS

NB performed data acquisition and analysis. JBA designed the study, performed data analysis and interpretation, and drafted the manuscript. VB contributed to the concept of the study and critically revised the manuscript. PNG designed the study, performed data interpretation, and drafted the manuscript. BH provided lab facilities and critically revised the manuscript.

REFERENCES

Adameyko, I., & Fried, K. (2016). The Nervous System Orchestrates and Integrates Craniofacial Development: A Review. *Frontiers in Physiology*, 7, 49.

Adams, D.C., Collyer, M.L. & Kaliontzopoulou, A. (2020) Geomorph: Software for geometric morphometric analyses. R package version 3.2.1. https://cran.r-project.org/package=geomorph.

Alamy, M., & Bengelloun, W. A. (2012). Malnutrition and brain development: an analysis of the effects of inadequate diet during different stages of life in rat. *Neuroscience and Biobehavioral Review*s, 36(6), 1463–1480.

Alatorre, J.L. Ponce de León, M.S., Hopkins, W.D. & Zollikofer, C.P.E. (2019) Evidence for independent brain and neurocranial reorganization during hominin evolution. *Proceedings of the National Academy of Sciences*, 116(44), 22115–22121.

Aristide, L., Furtado dos Reis, S., Machado, A.C., Lima, I., Lopes, R.T. & Perez, S.I. (2016) Brain shape convergence in the adaptive radiation of New World monkeys. *Proceedings of the National Academy of Sciences of the United States of America*, 113(8), 2158–2163.

Barbeito-Andrés, J., Gleiser, P.M., Bernal, V., Hallgŕimsson, B. & Gonzalez, P.N. (2018) Brain structural networks in mouse exposed to chronic maternal undernutrition. *Neuroscience*, 380, 14–26.

Barbeito-Andrés, J., Gonzalez, P.N. & Hallgrímsson, B. (2016) Prenatal development of skull and brain in a mouse model of growth restriction. *Revista Argentina de Antropología Biológica*, 18(1), 1-13.

Barboza, P.S., Parker, K.L. & Hume, I.D. (2009) Integrative Wildlife Nutrition. Berlin: Springer.

Black, R. E., Allen, L. H., Bhutta, Z. A., Caulfield, L. E., de Onis, M., Ezzati, M., Mathers, C., Rivera, J., & Maternal and Child Undernutrition Study Group (2008). Maternal and child undernutrition: global and regional exposures and health consequences. *Lancet*, 371(9608), 243–260.

Bourke, C. D., Jones, K., & Prendergast, A. J. (2019). Current Understanding of Innate Immune Cell Dysfunction in Childhood Undernutrition. *Frontiers in Immunology*, 10, 1728.

Brameld J. M. (2004). The influence of undernutrition on skeletal muscle development. *The British Journal of Nutrition*, 91(3), 327–328.

Cohen, E., Baerts, W., & van Bel, F. (2015). Brain-Sparing in Intrauterine Growth Restriction: Considerations for the Neonatologist. *Neonatology*, 108(4), 269–276.

Cooke, R.W.I., Lucas, A., Yudkin, P.L.N. & Pryse-Davies, J. (1977) Head circumference as an index of brain weight in the fetus and newborn. *Early Human Development*, 1(2), 145-149.

Dressino, V. Pucciarelli, H. M. (1997). Cranial growth in Saimiri sciureus (Cebidae) and its alteration by nutritional factors: A longitudinal study. *American Journal of Physical Anthropology,* 102(4), 545-554.

Fedorov, A., Beichel, R., Kalpathy-Cramer, J., Finet, J., Fillion-Robin, J-C., Pujol, S. & et al. (2012) 3D Slicer as an Image Computing Platform for the Quantitative Imaging Network. *Magnetic Resonance Imaging*, 30(9), 1323–1341.

Fournier, M., Combès, B., Roberts, N., Braga, J. & Prima, S. (2011) Mapping the distance between the brain and the inner surface of the skull and their global asymmetries. *Medical Imaging 2011: Image Processing*, 7962, 79620Y.

Georgieff M. K. (2007). Nutrition and the developing brain: nutrient priorities and measurement. The *American Journal of Clinical Nutrition*, 85(2), 614S–620S.

Gómez-Robles, A., Reyes, L.D. & Sherwood, C. (2018) Landmarking brains. In: Bruner, E., Ogihara, N., Tanabe, H.C. (Ed.) *Digital endocasts. From skulls to brains*. Tokyo: Springer, pp. 115–126.

Gonda, A., Välimäki, K., Herczeg, G. & Merilä, J. (2012) Brain development and predation: plastic responses depend on evolutionary history. *Biology Letters*, 8, 249–252.

Gonzalez, P.N., Gasperowicz, M., Barbeito-Andrés, J., Klenin, N., Cross, J.C. & Hallgŕımsson, B. (2016) Chronic protein restriction in mice impacts placental function and maternal body weight before fetal growth. *PLoS ONE* 11, e0152227.

Gonzalez, P. N., Kristensen, E., Morck, D. W., Boyd, S., & Hallgrímsson, B. (2013). Effects of growth hormone on the ontogenetic allometry of craniofacial bones. *Evolution & Development*, 15(2), 133–145.

Gonzalez, P. N., Oyhenart, E. E. & Hallgrimsson, B. (2011) Effects of environmental perturbations during postnatal development on the phenotypic integration of the skull. *Journal Of Experimental Zoology Part B-molecular And Developmental Evolution*, 316 B, 547–561.

Gunz, P. & Mitteroecker, P. (2013). Semilandmarks: a method for quantifying curves and surfaces. *Hystrix, the Italian Journal of Mammalogy*, 24(1), 103-109.

Gunz, P., Mitteroecker, P. & Bookstein, F.L. (2005) Semilandmarks in Three Dimensions. In: Slice, D.E. (Ed.) *Modern Morphometrics in Physical Anthropology*. *Developments in Primatology: Progress and Prospects*. Boston: Springer, pp. 73–98.

Hanken, J. & Thorogood, P. (1993) Evolution and development of the vertebrate skull—the role of pattern formation. *Trends in Ecology and Evolution*, 8(1), 9–15.

Hill, C.A., Martínez-Abadías, N., Motch, S.M., Austin, J.R., Wang, Y., Jabs, E.W. & et al. (2013) Postnatal brain and skull growth in an Apert syndrome mouse model. *American Journal of Medical Genetics Part A*, 161A, 745–757.

Hunter, D. S., Hazel, S. J., Kind, K. L., Owens, J. A., Pitcher, J. B., & Gatford, K. L. (2016). Programming the brain: Common outcomes and gaps in knowledge from animal studies of IUGR. *Physiology & Behavior*, 164(Pt A), 233–248.

Kotrschal, A., Deacon, A.E., Magurran, A.E. & Kolm, N. (2017) Predation pressure shapes brain anatomy in the wild. *Evolutionary Ecology*, 31, 619–633.

Lieberman, D. E., Hallgrímsson, B., Liu, W., Parsons, T. E., & Jamniczky, H. A. (2008). Spatial packing, cranial base angulation, and craniofacial shape variation in the mammalian skull: testing a new model using mice. *Journal of Anatomy*, 212(6), 720–735.

Marcucio, R., Hallgrímsson, B. & Young, N.M. (2015) Facial Morphogenesis: Physical and Molecular Interactions Between the Brain and the Face. *Current Topics in Developmental Biology*, 115, 299–320.

Marcucio, R. S., Young, N. M., Hu, D., & Hallgrimsson, B. (2011). Mechanisms that underlie co-variation of the brain and face. *Genesis*, 49(4), 177–189.

Martínez-Abadías, N., Heuze, Y., Wang, Y., Jabs, E.W., Aldridge, K., et al. (2011) FGF/FGFR Signaling Coordinates Skull Development by Modulating Magnitude of Morphological Integration: Evidence from Apert Syndrome Mouse Models. *PLoS ONE* 6(10), e26425.

Marugan-Lobon, J., Watanabe, A. & Kawabe, S. (2016) Studying avian encephalization with geometric morphometrics. *Journal of Anatomy*, 229(2), 191–203.

Miller, S. L., Huppi, P. S., & Mallard, C. (2016). The consequences of fetal growth restriction on brain structure and neurodevelopmental outcome. *The Journal of Physiology*, 594(4), 807–823.

Moss, M.L. & Young, R.W. (1960) A functional approach to craniology. *American Journal of Physical Anthropology*, 18, 281–291.

Motch Perrine, S.M., Stecko, T., Neuberger, T., Jabs, E.W., Ryan, T.M. & Richtsmeier, J.T. (2017) Integration of Brain and Skull in Prenatal Mouse Models of Apert and Crouzon Syndromes. *Frontiers in Human Neuroscience,* 25(11), 369.

Neubauer, S., Gunz, P. & Hublin, J.J. (2010) Endocranial shape changes during growth in chimpanzees and humans: A morphometric analysis of unique and shared aspects. *Journal of Human Evolution*, 59, 555–566.

Nieman, B.J., Blank, M.C., Roman, B.B., Henkelman, R.M. & Millen, K.J. (2012) If the skull fits: magnetic resonance imaging and microcomputed tomography for combined analysis of brain and skull phenotypes in the mouse. *Physiological Genomics*, 44, 992–1002.

Nijhout, H.F. (2003) Development and evolution of adaptive polyphenisms. *Evolutionary Development*, 5(1), 9–18.

Oksanen, J., Blanchet, F.G., Kindt, R., et al. (2015). Vegan: community ecology package. R package vegan, vers. 2.2-1.

Pereira-Pedro, A.S & Bruner, E. Landmarking endocasts. In: Bruner, E., Ogihara, N., Tanabe, H.C. (Ed.) *Digital endocasts. From skulls to brains*. Tokyo: Springer, pp. 127–142.

Peres-Neto, P. R., & Jackson, D. A. (2001). How well do multivariate data sets match? The advantages of a Procrustean superimposition approach over the Mantel test. *Oecologia*, 129(2), 169–178.

Pucciarelli, H. M., & Oyhenart, E. E. (1987). Effects of maternal food restriction during lactation on craniofacial growth in weanling rats. *American Journal of Physical Anthropology*, 72(1), 67–75.

Prado, E. L., & Dewey, K. G. (2014). Nutrition and brain development in early life. *Nutrition reviews*, 72(4), 267–284.

Profico, A., Schlager, S., Valoriani, V., Buzi, C., Melchionna, M., Veneziano, A. & et al. (2018) Reproducing the internal and external anatomy of fossil bones: Two new automatic digital tools. *American Journal of Physical Anthropology*, 166(4), 979–986.

R Core Team (2020). R: A language and environment for statistical computing. *R Foundation for Statistical Computing*. https://www.R-project.org/

Reichling, T.D. & German, R.Z. (2000) Bones, muscles and visceral organs of protein-malnourished rats (Rattus norvegicus) grow more slowly but for longer durations to reach normal final size. *Journal of Nutrition*, 130, 2326–2332.

Richtsmeier J. & Flaherty, K. (2013) Hand in glove: brain and skull in development and dysmorphogenesis. *Acta Neuropathologica*, 125, 469–489.

Richtsmeier, J.T., Aldridge, K., DeLeon, V.B., Panchal, J., Kane AA, Marsh, J.L. & et al., (2006) Phenotypic integration of neurocranium and brain. *Journal of Experimental Zoology Part B*, 306B(4), 360–378.

Rohlf, F. J. & Corti, M. 2000. Use of Two-Block Partial Least-Squares to Study Covariation in Shape. *Systematic Biology*, 49, 740–753.

Schlager, S. (2017) Morpho and Rvcg – Shape Analysis in R. In: Zheng, G., Li, S., Szekely, G. (Ed.) *Statistical Shape and Deformation Analysis*. Academic Press, pp. 217–256.

Scholz, J., LaLiberté, C., van Eede, M., Lerch, J.P. & Henkelman, M. (2016) Variability of brain anatomy for three common mouse strains. *Neuroimage*, 142, 656–662.

Shattuck, DW. & Leahy, R.M. (2002) BrainSuite: An Automated Cortical Surface Identification Tool. *Medical Image Analysis*, 6(2), 129–142.

Ulijaszek S. J. (1996). Energetics, adaptation, and adaptability. *American journal of human biology : the official journal of the Human Biology Council*, 8(2), 169–182.

Watanabe, A., Gignac, P.M. Balanoff, A.M., Green, T.L., Kley, N.J. & Norell, M.A. (2019) Are endocasts good proxies for brain size and shape in archosaurs throughout ontogeny? *Journal of Anatomy*, 234, 291–305.

Wiley, D.F., Amenta, N., Alcantara, D.A., Ghosh, D., Kil, Y.J., Delson, E. & et al. (2005) Evolutionary morphing. In: Silva, C.T., Groeller, E., Rushmeier, H.E. (Ed.) *IEEE Visualization*. California: Computer Society Press, pp. 431-438.

Yu, J.C., Lucas, J.H., Fryberg, K. & Borke, J.L. (2001) Extrinsic tension results in FGF-2 release, membrane permeability change, and intracellular Ca++ increase in immature cranial sutures. *Journal of Craniofacial Surgery*, 12(4), 391–398.

LEGENDS TO FIGURES

Figure 1. (A) Endocast reconstruction from microCT images. Illustrative example of a microCT coronal slice showing bone structures of the skull (left), scale bar = 1 mm. Skull tridimensional reconstruction and landmarks digitized to perform automatic extraction of the endocast as explained in Profico et al., (2018) (middle). Endocast tridimensional reconstruction obtained after endocranial segmentation (right). (B) Brain reconstruction from MRI. Illustrative example of an MRI coronal slice, scale bar = 1 mm. Brain tissues are indicated as a shaded area (left). Brain tridimensional reconstruction obtained after segmentation (right). (C) Landmarks and semilandmarks digitized to assess morphological variation in the brains and the endocasts. For more details on digitized points, see Table 1.

Figure 2. Brain and endocranial size variation. (A) Inter-sample variation in brain and endocranial volume. (B) Scatter plot and regression lines of brain vs. endocranial volumes. Lines were obtained from regressions performed for each experimental treatment (Co: r2 = 0.814**, LCP: r2 = 0.538, LP: r2 = 0.850**). (C) Observed and estimated brain volumes for LCP and LP. The estimated values were computed using the linear function from Co group: brain volume (mm3) = 0.99 * endocast volume (mm3) - 51.24. Co = Control group, LCP = Low calorie-protein group, LP = Low protein group. *p < 0.05, **p < 0.01, ***p < 0.001.

Figure 3. Shape variation within and between brains and endocasts. (A) Procrustes distance between corresponding endocasts and brains of each specimen (left), shape variation between brains (middle) and endocasts (right) within the experimental groups. ANOVA resulted in significant difference between these categories of Procrustes distances ($F = 10.987$, $p < 0.0001$). For details on paired comparison, Tukey post-hoc results are presented in Table 2. (B-D) Morphings represent the endocast (left) and brain (right) configurations for the same specimen, which is around the mean value of Procrustes brain-endocast. For each experimental group, the specimen that was closer to the average in the distribution of "Brain-endocast difference" was chosen and its coordinates were used to illustrate the shape configuration of both structures.

Figure 4. PCA on brain and endocast shape data. Distribution of specimens along PC1 and PC2 derived from PCA on brain (A) and endocast (B) shape coordinates. Morphings illustrate PC1 negative and positive extremes. Heatmaps show the distances between the shapes at the extremes of PC1.

Figure 5. PLS on brain and endocast shape data. (A) Distribution of specimens along PLS1 for coordinates of the endocast and the brain blocks. Morphings illustrate shape configurations in negative and positive extremes of PLS1 for each block. (B) In order to better capture shape differences along PLS1, coordinates corresponding to the negative (gray) and positive (black) extremes of each block in PLS1 are presented.

Figure 6. Brain and endocast shape asymmetry. (A) Overall shape asymmetry for the brain and endocast. (B) PCA of the asymmetric component for the brain (left) and endocast (right), heatmaps represent the variation along PC1. The heatmaps show the distances between the symmetric mean shape and the positive extreme of PC1, blue surfaces represent larger areas and red surfaces smaller areas compared to the mean.

TABLES

Curve	Initial extreme landmark	Final extreme landmark	Number of curve semilandmarks	Description
1	Most rostral point on interhemispheric fissure	Most caudal point on interhemispheric fissure	23	Curve lays along the interhemispheric fissure
2	Most caudal point on medial line of the cortex, right side	Ventro-lateral intersection between the occipital lobe and the cerebellum, right side	13	Curve extends along the caudal limit of the cortex, right side
3	Most caudal point on medial line of the cortex, left side	Ventro-lateral intersection between the occipital lobe and the cerebellum, left side	13	Curve extends along the caudal limit of the cortex, left side
4	Most rostral point in the intersection between the right and left olfactory bulbs	Most caudal point in the intersection between the right and left olfactory bulbs	8	Curve corresponds to the sagittal fissure between both olfactory bulbs
5	Rostral and medial point on the olfactory bulb at the intersection with the fissure between olfactory bulbs, right side	Most caudal point in the lateral limit of the olfactory bulb, right side	8	Curve extends along the lateral border of the olfactory bulb, right side
6	Rostral and medial point of the olfactory bulb at the intersection with the fissure between olfactory bulbs, left side	Most caudal point in the lateral limit of the olfactory bulb, left side	8	Curve extends along the lateral border of the olfactory bulb, right side
7	Most rostral and lateral point at the intersection of olfactory bulb with anterior frontal lobe, right side	Caudo-lateral point of occipital lobe, right side	23	Curve lays along the lateral cortical border, right side

8	Most rostral and lateral point at the intersection of olfactory bulb with anterior frontal lobe, left side	Caudo-lateral point of occipital lobe, left side	23	Curve lays along the lateral cortical border, left side
9	Most rostral point of the colliculus at the intersection with the interhemispheric fissure	Most caudal point of the cerebellum in the sagittal plane	18	Curve extends in the medial plane between the caudal limit of the cortex through the cerebellum
10	Intersection between the paraflocculus and the cerebellum, left side	Caudal point of the left hemicerebellar surface	13	Curve is placed in the lateral border of the cerebellum, left side
11	Intersection between the paraflocculus and the cerebellum, right side	Caudal point of the right hemicerebellar surface	13	Curve is placed in the lateral border of the cerebellum, right side
12	Rosto-lateral limit of the cerebellum, right side	Rosto-lateral limit of the cerebellum, left side	18	Curve extends along the dorsal surface of the cerebellum

Table 1. Curves of points digitized on brain and endocast surfaces. Extreme landmarks of the curves and the number of semilandmarks along the curves are indicated.

		Brain-endocast difference			Brain variation			Endocast variation		
		Co	LCP	LP	Co	LCP	LP	Co	LCP	LP
Brain-endocast difference	Co		0.0239*	0.0104	0.0264***	0.0345***	0.0366***	0.0327***	0.0433***	0.0266***
	LCP	0.023		-0.0135	0.0025	0.0106	0.0127	0.0088	0.0194	0.0027
	LP	0.828	0.632		0.016	0.0241**	0.0262***	0.0223**	0.0329***	0.0162
Brain variation	Co	<0.0001	0.999	0.092		0.0081	0.0102	0.0063	0.0169**	0.0002
	LCP	<0.0001	0.75	0.003	0.577		0.0021	-0.0018	0.0088	-0.0008
	LP	<0.0001	0.464	<0.0001	0.145	0.999		-0.0039	0.0067	-0.01
Endocast variation	Co	<0.0001	0.846	0.002	0.66	0.999	0.981		0.0106	-0.0061
	LCP	<0.0001	0.057	<0.0001	0.002	0.64	0.841	0.218		-0.0167**
	LP	<0.0001	0.999	0.107	0.999	0.678	0.236	0.778	0.006	

Table 2. Post-hoc comparisons for ANOVA on Procrustes distances. Tuckey results for paired comparisons are presented as the mean difference (above diagonal) and the p-value (below diagonal). *p < 0.05, **p < 0.01, ***p < 0.001.

SUPPORTING INFORMATION

Figure S1. PCA on superimposed coordinated of the error test.

Figure S2. Figure S2. Error test. Procrustes distances.

Table S1. Error test. Paired t-test on PC1 and PC2 scores.

Table S2. Effect of litter size. ANOVA with litter size as covariate.

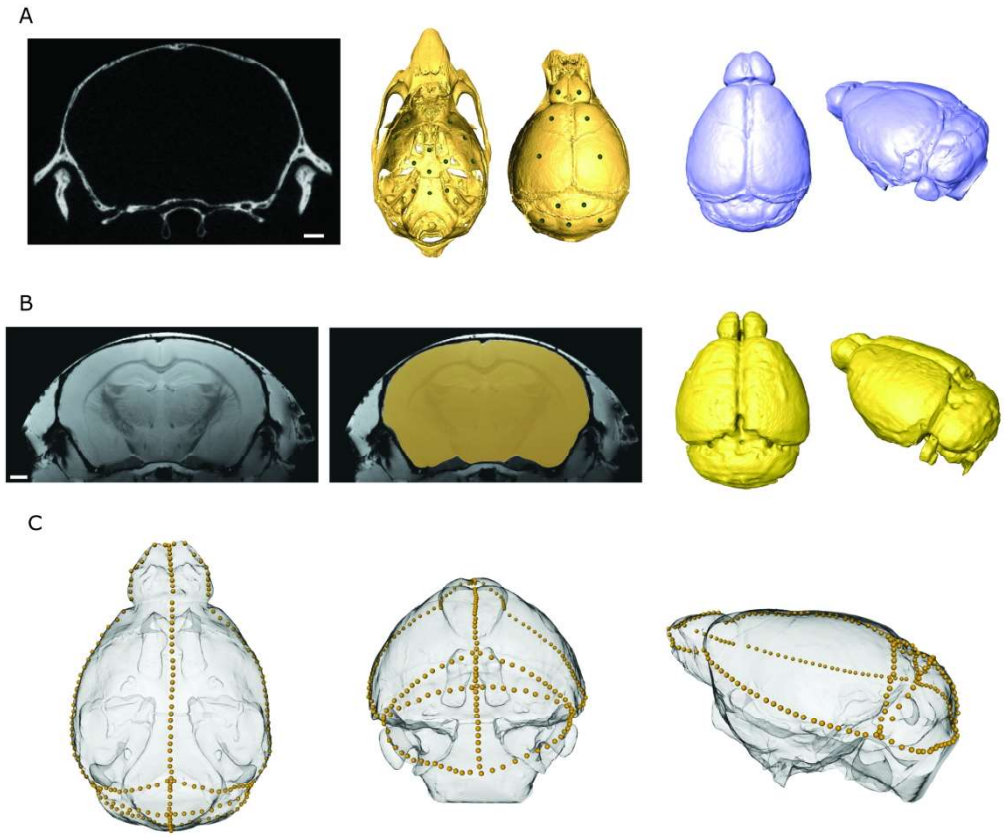

(A) Endocast reconstruction from microCT images. Illustrative example of a microCT coronal slice showing bone structures of the skull (left), scale bar = 1 mm. Skull tridimensional reconstruction and landmarks digitized to perform automatic extraction of the endocast as explained in Profico et al., (2018) (middle). Endocast tridimensional reconstruction obtained after endocranial segmentation (right). (B) Brain reconstruction from MRI. Illustrative example of an MRI coronal slice, scale bar = 1 mm. Brain tissues are indicated as a shaded area (left). Brain tridimensional reconstruction obtained after segmentation (right). (C) Landmarks and semilandmarks digitized to assess morphological variation in the brains and the endocasts. For more details on digitized points, see Table 1.

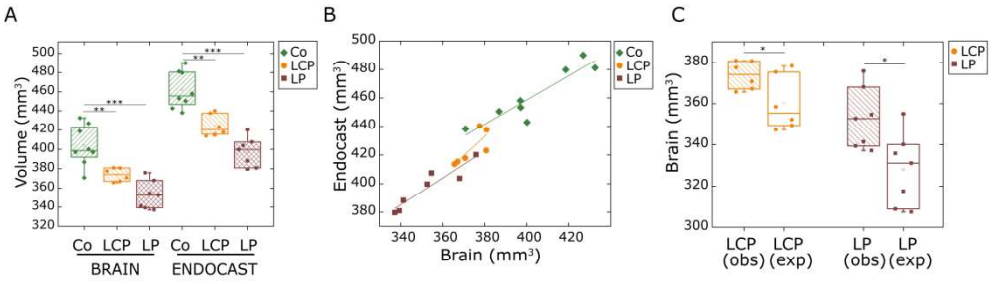

Brain and endocranial size variation. (A) Inter-sample variation in brain and endocranial volume. (B) Scatter plot and regression lines of brain vs. endocranial volumes. Lines were obtained from regressions performed for each experimental treatment (Co: r2 = 0.814**, LCP: r2 = 0.538, LP: r2 = 0.850**). (C) Observed and estimated brain volumes for LCP and LP. The estimated values were computed using the linear function from Co group: brain volume (mm3) = 0.99 * endocast volume (mm3) - 51.24. Co = Control group, LCP = Low calorie-protein group, LP = Low protein group. *p < 0.05, **p < 0.01, ***p < 0.001.

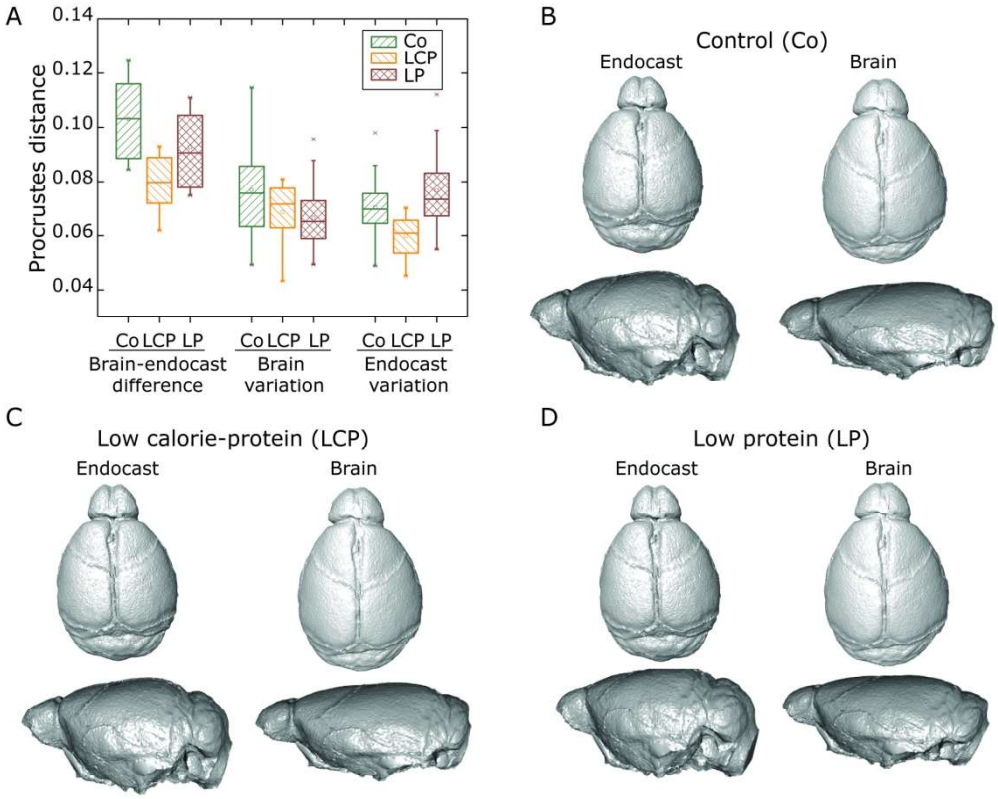

Shape variation within and between brains and endocasts. (A) Procrustes distance between corresponding endocasts and brains of each specimen (left), shape variation between brains (middle) and endocasts (right) within the experimental groups. ANOVA resulted in significant difference between these categories of Procrustes distances ($F=10.987$, $p<0.0001$). For details on paired comparison, Tukey post-hoc results are presented in Table 2. (B-D) Morphings represent the endocast (left) and brain (right) configurations for the same specimen, which is around the mean value of Procrustes brain-endocast distance in each group.

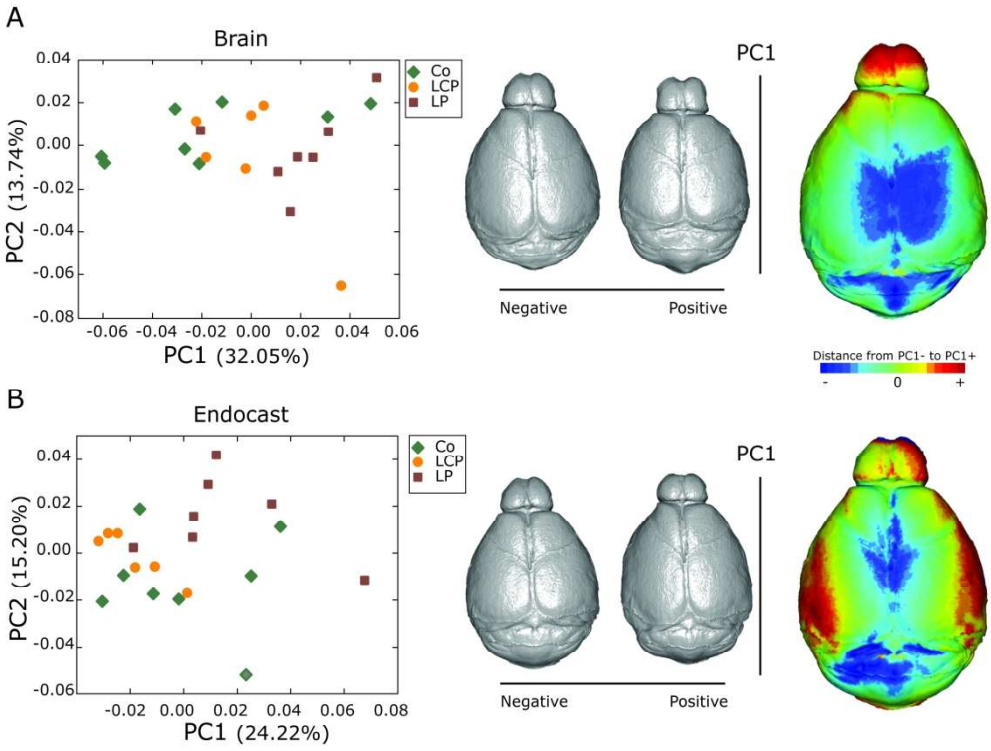

PCA on brain and endocast shape data. Distribution of specimens along PC1 and PC2 derived from PCA on brain (A) and endocast (B) shape coordinates. Morphings illustrate PC1 negative and positive extremes. Heatmaps show the distances between the shapes at the extremes of PC1.

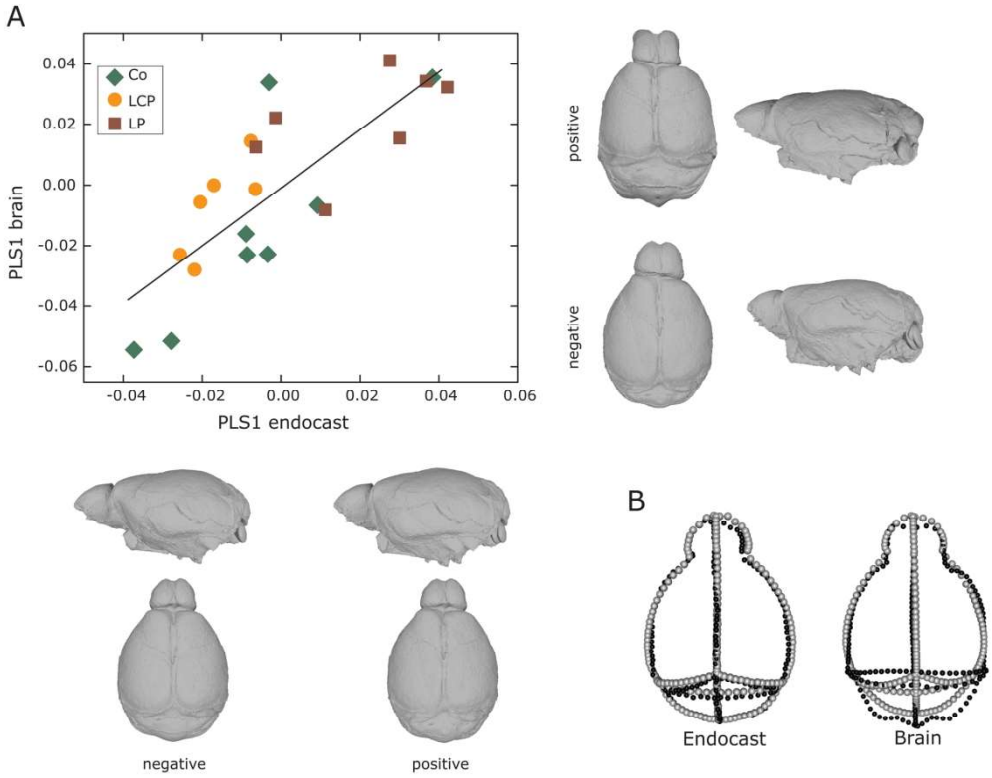

PLS on brain and endocast shape data. (A) Distribution of specimens along PLS1 for coordinates of the endocast and the brain blocks. Morphings illustrate shape configurations in negative and positive extremes of PLS1 for each block. (B) In order to better capture shape differences along PLS1, coordinates corresponding to the negative (gray) and positive (black) extremes of each block in PLS1 are presented.

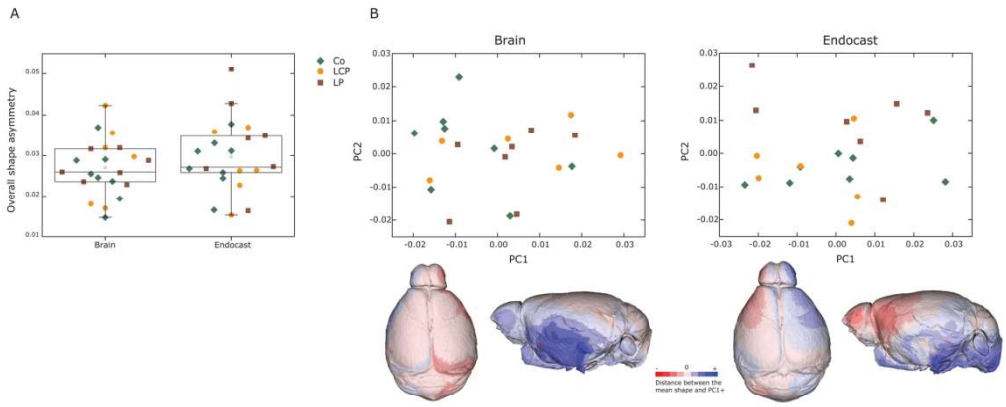

Brain and endocast shape asymmetry. (A) Overall shape asymmetry for the brain and endocast. (B) PCA of the asymmetric component for the brain (left) and endocast (right), heatmaps represent the variation along PC1. The heatmaps show the distances between the symmetric mean shape and the positive extreme of PC1, blue surfaces represent larger areas and red surfaces smaller areas compared to the mean.

SUPPORTING INFORMATION

Intra-observer error test

Coordinates on the brains and the endocast were digitized by the first author (NB). To assess the repeatability of this procedure, a preliminary intra-observer error test was performed. For this purpose, 10 specimens were randomly selected from our sample and the complete set of 205 landmarks and semilandmarks used in the study was digitized on their brains and endocast in two different measuring sessions. Both sessions were separated by 10 days.

First, on the superimposed coordinates, a Principal Component Analysis (PCA) was performed in order to explore the ordination of repeated measures along the main axes of variation. The first two axes account for ~50% of total variation.

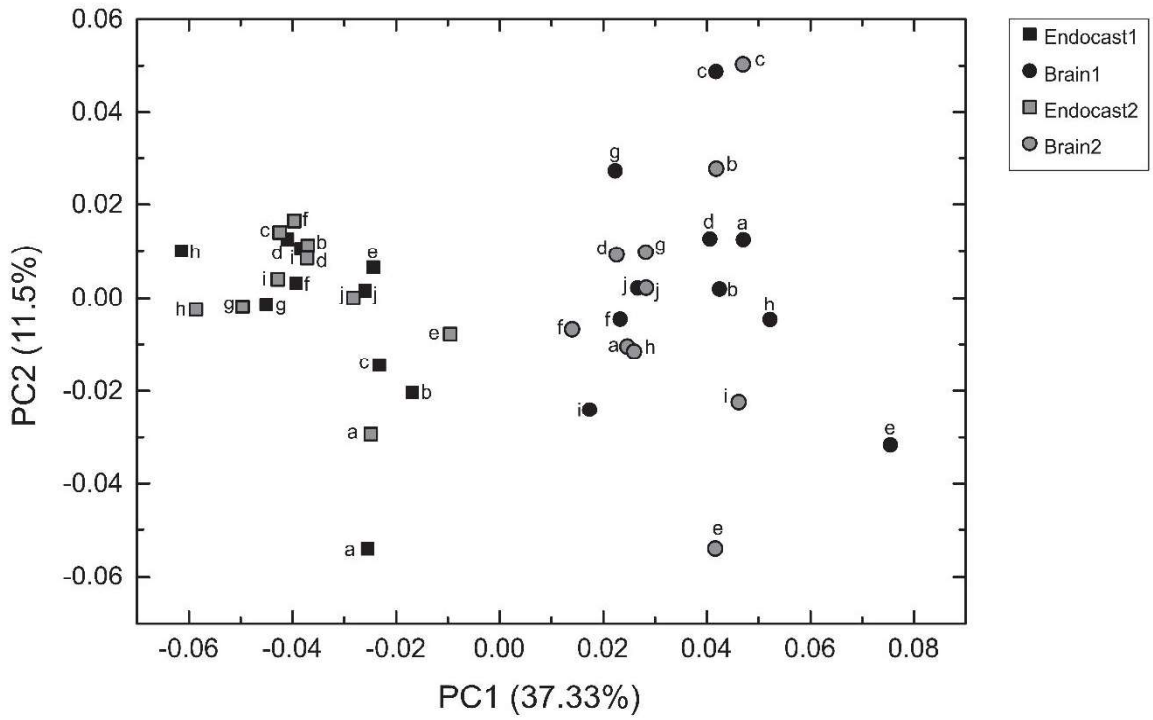

Figure S1. PCA on superimposed coordinated of the error test. Distribution along PC1 and PC2 is presented, and the amount of variation accounted by each axis is also showed. Each specimen included in the test is named by a consecutive letter (a-j). Each set of measurement is indicated using a different color, with black for the first set of digitization and grey for the second. Finally, the type of the structure is presented with different symbols: endocast (squares) and brains (circles).

As can be observed in Fig. S1, there is an evident separation between brains and endocast along PC1, with the latter occupying negative values. This result suggest that digitization error was not as

important as variation due to the type of anatomical structure. In addition, with some exceptions, repeated measurements of the same structure displayed a close placement in the space formed by PC1 and PC2, which indicates a qualitative similarity between the first and the second session of digitization.

As well, repeated measures were quantitatively compared using a paired t-test on PC1 and PC2 scores.

Table S1. Error test. Paired t-test on PC1 and PC2 scores.

	PC1	**PC2**
Endocast	t = 0.883, p= 0.400	t = -1.070, p = 0.313
Brain	t = 1.156, p = 0.276	t = 1.012, p = 0.338

Results obtained from the paired t-test suggest that there are not significant differences between the first and the second measurement for the compared scores.

Finally, we carried out comparisons on Procrustes distances to assess whether differences between repeated measurement were smaller or larger than differences between the brain and the endocast of the same specimen and between the brain or the endocast of different specimens.

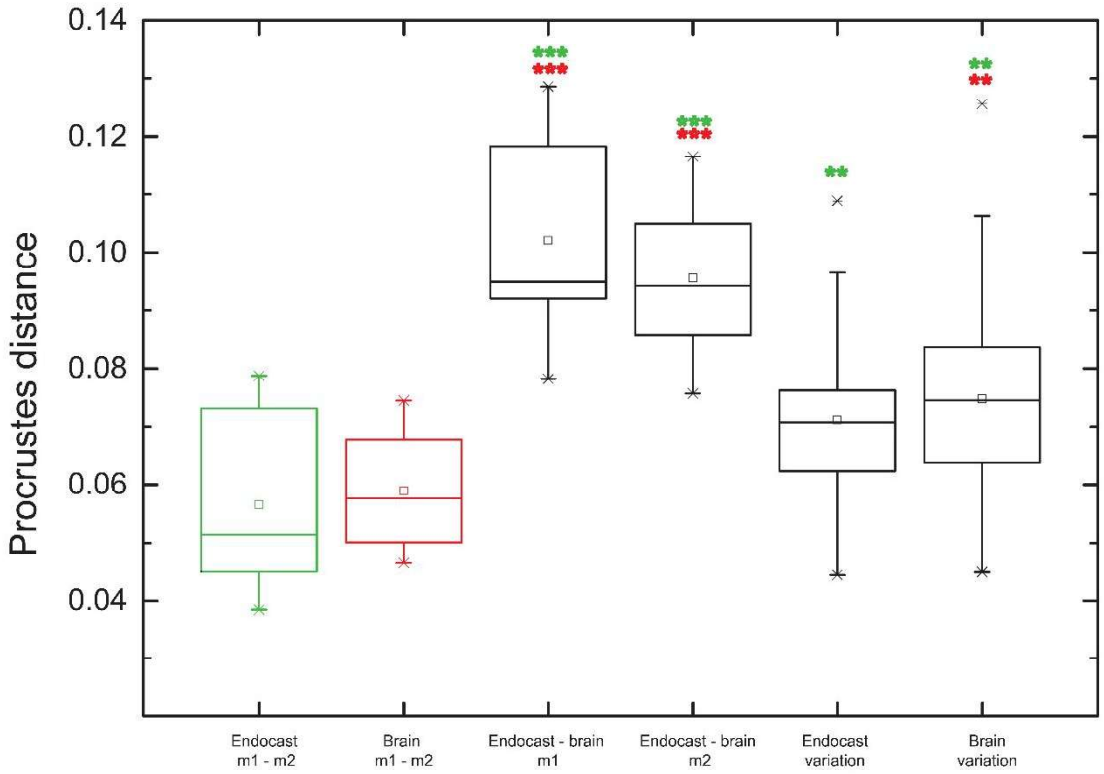

Figure S2. Error test. Procrustes distances. Distributions of Procrustes distances between repeated measures (m1 and m2) for the endocast (green) and brain (red) compared to distances between different structures of the same specimens and inter-specimen variation within the same structures. ANOVA resulted in highly significant differences between distances for these comparisons ($F = 18.57$, $p < 0.0001$). Tukey pairwise comparisons between distances for repeated measures and the other categories are illustrated, where green asterisks represent differences to the endocast repeated measures distance and the red to the brain. *$p < 0.05$, **$p < 0.01$, ***$p < 0.001$.

In general, Procrustes distances for repeated measures resulted smaller than brain-endocast distances for the same specimens, reinforcing previous results that suggest that digitization repeatability was robust enough to account for shape difference between types of tissues (brain and endocast). In the same line, although more modest, significant differences were found for distances between repeated measures and distances between different specimens. This indicates that digitization is reliable to describe inter-specimens variation in both structures.

Effect of litter size

In order to assess the impact of litter size in volume comparisons of the brain and the endocast, a preliminary ANOVA was performed using the litter size as a covariate. Results indicated that after controlling litter size, experimental treatment is still statistically significant.

Table S2. Effect of litter size. ANOVA with litter size as covariate

	Brain				**Endocast**			
	Sum of Squares	df	F value	p-value	Sum of Squares	df	F value	p-value
(Intercept)	333727	1	1140.349	<0.0001	438544	1	1458.332	<0.0001
Group	9428	2	16.109	0.00012	15212	2	25.294	<0.0001
Litter size	22	1	0.077	0.785	53	1	0.175	0.681